

An Accurate and Real-time Relative Pose Estimation from Triple Point-line Images by Decoupling Rotation and Translation

Zewen Xu^{1,2}, Yijia He³, Hao Wei^{1*}, Bo Xu⁴, BinJian Xie^{1,2} and Yihong Wu^{1,2*}

Abstract—Line features are valid complements for point features in man-made environments. 3D-2D constraints provided by line features have been widely used in Visual Odometry (VO) and Structure-from-Motion (SfM) systems. However, how to accurately solve three-view relative motion only with 2D observations of points and lines in real time has not been fully explored. In this paper, we propose a novel three-view pose solver based on rotation-translation decoupled estimation. First, a high-precision rotation estimation method based on normal vector coplanarity constraints that consider the uncertainty of observations is proposed, which can be solved by Levenberg-Marquardt (LM) algorithm efficiently. Second, a robust linear translation constraint that minimizes the degree of the rotation components and feature observation components in equations is elaborately designed for estimating translations accurately. Experiments on synthetic data and real-world data show that the proposed approach improves both rotation and translation accuracy compared to the classical trifocal-tensor-based method and the state-of-the-art two-view algorithm in outdoor and indoor environments.

I. INTRODUCTION

Line features have long been believed as a provably valid complement for point features in man-made environments [1], [2], which can significantly enhance the robustness of pose estimation, particularly in weak-texture scenarios. Consequently, they have been integrated into VO systems [3] and SfM systems [4] in recent years.

In existing point-line-based VO systems [2], [3], [5], [6] or SfM systems [4], line features mainly contribute to pose estimation with the correspondences between 3D landmarks and 2D observations [7], [8]. However, at the start of these systems, there are no 3D structures before triangulation. It means that an initial pose should be estimated only with 2D observations. Although a non-real-time relative pose solver with 2D points and lines has been proposed to address weak-texture cases in SfM applications [9], only point features are used to obtain the initial pose in most existing point-line-based VO systems [2], [3], [5], [6] due to the lack of an accurate and real-time point-line-based relative pose

estimator. There is no doubt that this absence will limit further applications of lines in VO systems.

For most applications of relative pose estimation in VO systems, the essential matrix is widely used in two-view calibrated cases. It can be estimated accurately and efficiently with five points [10], [11]. However, due to the mixing parameters of rotation and translation, these methods suffer from solution multiplicity, planar degeneracy, and pure rotation degeneracy [12], [13]. To settle these problems, Kneip *et al.* [12] proposed a solution that achieved decoupled estimation of rotation and translation by introducing an equivalent constraint to the essential matrix, known as the normal epipolar constraint (NEC). Their later work [13] provided a real-time solver for NEC. Besides, Muhle *et al.* [14] considered the position uncertainty of points and proposed a solution for the NEC problem with iteratively reweighted least square (IRLS) algorithm [15], called PNEC. These methods gradually get more attention and replace essential-matrix-based methods in odometry systems [16]–[18]. We extend this idea to the point-line-based cases.

When referring to line features without any priors, it is necessary to consider observations from at least three frames [19]. Three-view relative pose estimation is believed as a fallback when two-view pose estimation fails [20]. In theory, 6 lines or 4 points are enough to solve the calibrated three-view pose problems, known as minimal solutions [19]. However, these solvers yield much more spurious solutions than two-view minimal solvers due to more non-linear constraints and variables being introduced, thus believed as hard minimal problems [21]. As shown in [1], there might be up to 600 solutions under a 6-line configuration. Although Ding *et al.* [22] leveraged the Homotopy Continuation (HC) algorithm [23] to settle the multiple-solution problem, their algorithm cannot perform real-time calculations on CPU. For point-line cases, the minimal problems have just been completely classified in [24], [25]. In addition to facing multiple solutions, different point-line configurations also need to be discussed separately, further increasing the difficulties in practical applications. Fabbri *et al.* [9] proposed an HC-based method for solving two minimal problems among them. However, this method is still non-real-time. When considering more features, the solving process will become much easier. A classical approach is the trifocal-tensor-based method [19], which can lead to a real-time linear solver with no less than 13 lines, 7 points, or a mixture of them. However, it overlooks the non-linear internal constraints of rotations, consequently failing to deliver satisfactory accuracy. Besides, this method cannot handle planar or pure rotation degeneracy

*This work was supported by Beijing Science and Technology Plan Project Z231100007123005 and a SINOPEC Research Project. (Corresponding authors: Hao Wei and Yihong Wu.)

^{1,2}Zewen Xu, Hao Wei, Binjian Xie, and Yihong Wu are with the State Key Laboratory of Multimodal Artificial Intelligence Systems, Institute of Automation, Chinese Academy of Sciences, Beijing 100190, China. Zewen Xu, Binjian Xie and Yihong Wu are also with the School of Artificial Intelligence, University of Chinese Academy of Sciences, Beijing 100190, China (e-mail: {xuzewen2020; weihao2019; xiebinjia2022; yihong.wu}@ia.ac.cn).

³Yijia He is with TCL RayNeo, China (e-mail: heyijia2016@gmail.com)

⁴Bo Xu is with the School of Geodesy and Geomatics, Wuhan University, Wuhan 430079, China (e-mail: boxu1995@whu.edu.cn).

due to the mixing parameter problem.

The aforementioned state of affairs motivates us to design an accurate and real-time point-line-based relative pose estimation algorithm capable of addressing situations involving pure rotation or planar degeneracy. The contributions of this paper are summarized as follows:

- An accurate and **Real-Time** pose estimator with **Points** and **Lines** is proposed, which estimates **Rotation** and **Translation** separately, allowing it to handle pure rotation degeneracy and planar degeneracy, namely **RT²PL**.
- Two forms of coplanarity constraints for rotation estimation with lines are proposed. We prove that one form is superior to another on convergence through experiments. Then the better one is combined with NEC leading to a point-line-based rotation solver, which can be easily solved by LM algorithm in real time. Additionally, the cost function integrates position uncertainty of points and lines, improving resilience to noise.
- A novel point-line-based linear translation constraint is introduced, meticulously designed to minimize the degree of the product of rotation and feature observations, thereby enhancing the resilience against rotation estimation errors and observation noises.
- Extensive experiments on synthetic and real-world data demonstrate the effectiveness of RT²PL, which outperforms both the classical trifocal-tensor-based method and the state-of-the-art two-view algorithm in general and degeneracy cases.

II. ROTATION ESTIMATION

NEC [13] constructed by point observations leads to an estimator where the rotation is recovered in a decoupled way. Inspired by it, for line features, normal back-projected constraint (NBC) is proposed in this paper. Integrating them and considering observation uncertainty results in a probability-aware point-line-based rotation estimation method.

A. Background-NEC

The observations in two images of a 3D points are set as ${}^k\mathbf{f}$, $k = 0, 1$, whose homogeneous coordinates ${}^k\bar{\mathbf{f}}$ are

$${}^k\bar{\mathbf{f}} = [{}^k u \quad {}^k v \quad 1]^T, \quad k = 0, 1. \quad (1)$$

The unit bearing vector corresponding to ${}^k\mathbf{f}$ is

$${}^k\mathbf{b} = \frac{\mathbf{K}^{-1}{}^k\bar{\mathbf{f}}}{\|\mathbf{K}^{-1}{}^k\bar{\mathbf{f}}\|_2}, \quad (2)$$

where \mathbf{K} is the camera intrinsics matrix. The epipolar plane corresponding to the 3D point is defined by its two bearing vectors. The normal vector of the epipolar plane represented in frame 0 is obtained by

$${}^0\mathbf{n} = {}^0\mathbf{b} \times \mathbf{R}_{01}{}^1\mathbf{b} \quad (3)$$

where $\mathbf{R}_{ab} \in SO(3)$ denotes the rotation that takes 3D features from frame b to frame a . The normal vectors of all these epipolar planes span a plane orthogonal to the direction of translation between two frames. The direction of

the translation represented in frame 0 is ${}^0\mathbf{t}_1$ (see Fig. 1(a)). NEC constraint enforces the coplanarity of normal vectors of epipolar planes and builds the following error:

$${}^0e = |{}^0\mathbf{t}_1^T {}^0\mathbf{n}|. \quad (4)$$

Assuming the number of 3D points that are observed by the two frames is m , the sum of the squares of these errors is

$$\mathbf{E}_{point} = \sum_{j=1}^m {}^0e_j^2 = {}^0\mathbf{t}_1^T {}^0\mathbf{M} {}^0\mathbf{t}_1, \quad (5)$$

where

$${}^0\mathbf{M} = \sum_{j=1}^m {}^0\mathbf{n}_j {}^0\mathbf{n}_j^T. \quad (6)$$

Minimizing Eq. (5) is equal to minimizing the minimal eigenvalue of ${}^0\mathbf{M}$, denoted by $\lambda_{0\mathbf{M}}^{min}$,

$$\mathbf{R}_{01} = \arg \min_{\mathbf{R}_{01}} \mathbf{E}_{point} = \arg \min_{\mathbf{R}_{01}} \lambda_{0\mathbf{M}}^{min}, \quad (7)$$

Eq. (7) is the core of decoupled rotation estimation.

B. Normal Back-projected Constraint

We propose NBC for rotation estimation with lines. 2D observation of a 3D line in the k -th image is represented as ${}^k\mathbf{l}$ with its polar coordinates $[{}^k\rho, {}^k\theta]$,

$${}^k\mathbf{l} = [\sin {}^k\theta \quad -\cos {}^k\theta \quad {}^k\rho]^T. \quad (8)$$

The back-projected plane that passes through the k -th camera optical center and ${}^k\mathbf{l}$ is represented as ${}^k\boldsymbol{\pi}_k = [{}^k\mathbf{n}_k^T, 0]^T$, where ${}^k\mathbf{n}_k$ is normal unit vector of the plane,

$${}^k\mathbf{n}_k = \frac{\mathbf{K}^T {}^k\mathbf{l}}{\|\mathbf{K}^T {}^k\mathbf{l}\|_2}. \quad (9)$$

If all normal vectors of back-projected planes corresponding to the line landmark are represented in a unified coordinate system (frame 1 for example), they will span a plane orthogonal to the direction of the landmark ${}^1\mathbf{r}$ (see Fig. 1(b)). Therefore, the error of the model can be built as below,

$${}^1e_k = |{}^1\mathbf{r}^T {}^1\mathbf{n}_k| = |{}^1\mathbf{r}^T \mathbf{R}_{1k} {}^k\mathbf{n}_k|, \quad (10)$$

where ${}^1\mathbf{n}_k$ denotes the normal vector of the k -th back-projected plane represented in frame 1. Each line correspondence across three frames can provide a coplanarity constraint. Assuming the number of 3D lines that can be observed by three frames is n . The cost function can be constructed similarly to NEC as below,

$$\mathbf{E}_{line} = \sum_{i=1}^n \sum_{k=0}^2 {}^1e_{k,i}^2 = \sum_{i=1}^n {}^1\mathbf{r}_i^T {}^1\mathbf{M}_i {}^1\mathbf{r}_i = \sum_{i=1}^n \lambda_{1\mathbf{M}_i}^{min}, \quad (11)$$

where

$${}^1\mathbf{M}_i = \sum_{k=0}^2 {}^1\mathbf{n}_{k,i} {}^1\mathbf{n}_{k,i}^T. \quad (12)$$

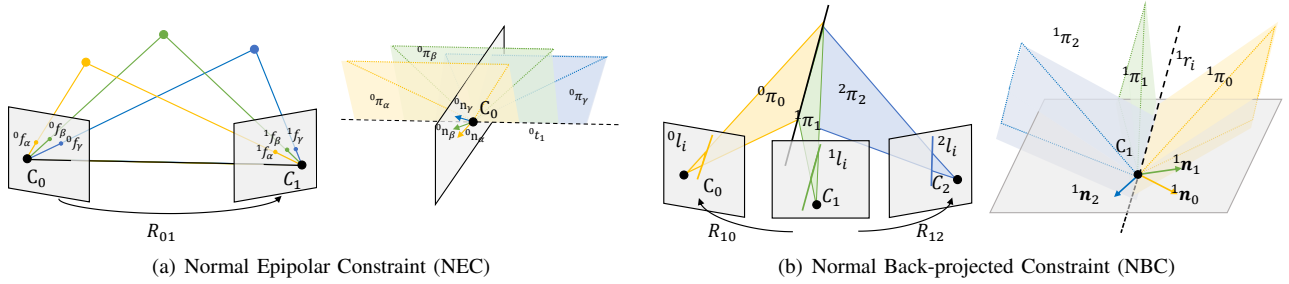


Fig. 1. **Geometry of the Constraints** (a) For clarity, we only show a constraint provided by three correspondences (α , β , and γ) in two frames. (b) For clarity, we only show a constraint provided by a line across three frames.

We still use $\lambda_{1M_i}^{min}$ denoting the minimal eigenvalue of 1M_i . Enforcing each error item led by n coplanarity constraints to zero, the problem can be solved by

$$[\mathbf{R}_{10} \ \mathbf{R}_{12}] = \arg \min_{[\mathbf{R}_{10} \ \mathbf{R}_{12}]} \begin{bmatrix} \lambda_{1M_1}^{min} \\ \lambda_{1M_2}^{min} \\ \vdots \\ \lambda_{1M_n}^{min} \end{bmatrix}. \quad (13)$$

It is worth noticing that, under the aforementioned constraints, there is no need to have any prior information about 3D lines, such as the directions of lines 1r_i , which are the eigenvectors related to those minimal eigenvalues.

Another Form for NBC: The coplanarity constraint can be built in another error form:

$$\begin{aligned} {}^1e_i &= |{}^1\mathbf{n}_0^T ({}^1\mathbf{n}_1 \times {}^1\mathbf{n}_2)| \\ &= |({}^1\mathbf{n}_0 \ {}^1\mathbf{n}_1 \ {}^1\mathbf{n}_2)| \\ &= |({}^1\mathbf{N}_i)|, \end{aligned} \quad (14)$$

where ${}^1\mathbf{N}_i$ is a matrix constructed by ${}^1\mathbf{n}_0$, ${}^1\mathbf{n}_1$, and ${}^1\mathbf{n}_2$. It has the following relationship with 1M_i in Eq. (12):

$${}^1M_i = {}^1\mathbf{N}_i^T {}^1\mathbf{N}_i. \quad (15)$$

Therefore,

$${}^1e_i = \sqrt{|{}^1M_i|} = \sqrt{\prod \lambda_{1M_i}}. \quad (16)$$

The sum of squares of these residuals is given by

$$\mathbf{E}_{line} = \sum_{i=1}^n {}^1e_i^2 = \sum_{i=1}^n (\prod \lambda_{1M_i}). \quad (17)$$

Enforcing each error item to zero, the problem is built as

$$[\mathbf{R}_{10} \ \mathbf{R}_{12}] = \arg \min_{[\mathbf{R}_{10} \ \mathbf{R}_{12}]} \begin{bmatrix} \prod \lambda_{1M_1} \\ \prod \lambda_{1M_2} \\ \vdots \\ \prod \lambda_{1M_n} \end{bmatrix}. \quad (18)$$

We call these two forms of NBC as minimal eigenvalue form (Eq. (13), **NBC-mini**) and eigenvalue multiplication form (Eq. (18), **NBC-mult**), respectively. The geometric meaning of one item in NBC-mini is the sum of squares of distances between the unit normal vectors and the fitted plane. The geometric meaning of one item in NBC-mult is the volume of the parallelepiped constructed by the three unit vectors. The experiments in Sec. IV-A will show that the NBC-mult form outperforms the NBC-mini form on the behavior of the cost function and the initial value resilience.

C. Rotation Part of RT^2PL

Considering three frames with m point correspondences and n line correspondences, the total cost function is the combination of Eq. (5) and Eq. (17):

$$\begin{aligned} \mathbf{E}(\mathbf{R}_{10}, \mathbf{R}_{12}) &= \mathbf{E}_{point}(\mathbf{R}_{10}) + \mathbf{E}_{point}(\mathbf{R}_{12}) \\ &\quad + \mathbf{E}_{line}(\mathbf{R}_{10}, \mathbf{R}_{12}). \end{aligned} \quad (19)$$

Although Eq. (19) enforces the coplanarity of normals of epipolar planes and the coplanarity of normals of back-projected planes, the importance of different features in the cost function is ignored, which has a significant impact on the estimator's performance [14]. According to Eq. (17), it is observed that the cost function constructed by lines is in the form of the sum of squared errors, similar to the point-based method Eq. (5). Each error term is only related to a single correspondence. Therefore, an IRLS version for solving the NBC problem, named PNBC, can be constructed naturally in a similar way to the PNEC [14]. To avoid the affection of occlusion and fragmentation problems, we model the uncertainty of line features as our previous work [26] and set the vertical uncertainty as σ_{line}^2 , then the covariance of line observation is given by

$$\Lambda_{k_{l_i}} = \begin{bmatrix} \frac{2}{c^2} \sigma_{line}^2 & -\frac{2d}{c^2} \sigma_{line}^2 \\ -\frac{2d}{c^2} \sigma_{line}^2 & \left(\frac{1}{2} + \frac{2d^2}{c^2}\right) \sigma_{line}^2 \end{bmatrix}, \quad (20)$$

where c is the line segment length, and d is the distance from the foot point to the midpoint of the line segment. The covariance of the normal vector of the back-projected plane $\Lambda_{k_{\mathbf{n}_{k,i}}}$ can be given by the unscented transform [27] according to Eq. (8). The weight of the error item related to the i -th line is

$$w_{line,i} = (\sigma_i^2)^{-1} = \left(\sum_{k=0}^2 \frac{\partial e_i}{\partial \mathbf{n}_{k,i}}^T \Lambda_{k_{\mathbf{n}_{k,i}}} \frac{\partial e_i}{\partial \mathbf{n}_{k,i}} \right)^{-1}. \quad (21)$$

Considering the point weights w_{point} , obtained by the inverse of the variance of residual (Eq. (4) in [14]), together, the IRLS version of Eq. (19) is

$$\begin{aligned} \mathbf{E}(\mathbf{R}_{10}, \mathbf{R}_{12}) &= \sum_{j=1}^{m_{10}} w_{point,j}^{(01)} {}^1e_j^2(\mathbf{R}_{10}) + \sum_{j=1}^{m_{12}} w_{point,j}^{(12)} {}^1e_j^2(\mathbf{R}_{12}) \\ &\quad + \sum_{i=1}^n w_{line,i} {}^1e_i^2(\mathbf{R}_{10}, \mathbf{R}_{12}). \end{aligned} \quad (22)$$

All of the weights are initialized as 1, and when the optimization solved by LM algorithm is convergent, the weight of each item will be updated with new estimated rotations.

III. TRANSLATION ESTIMATION

Whatever point or line features, the constraints about the translation will be linear when rotation is known. To build a linear constraint for translation with points and lines together, at least three frames should be considered. We set the general form of the constraint of translation among three frames as

$$\mathbf{B}^G \mathbf{t}_0 + \mathbf{C}^G \mathbf{t}_1 + \mathbf{D}^G \mathbf{t}_2 = \mathbf{0}, \quad (23)$$

where \mathbf{B} , \mathbf{C} , and \mathbf{D} denote coefficient matrix defined by rotations and feature correspondences, ${}^G \mathbf{t}_0$, ${}^G \mathbf{t}_1$, and ${}^G \mathbf{t}_2$ denote the global translation about frame 0, 1, and 2 respectively. We extend the concept in [28] and call the constraints similar to Eq. (23) as linear global translation (LiGT) constraints whatever the type of observations. Intuitively, when the degree of rotation components and observation components are lower, the impact of rotation estimation errors and the noise of observations on translation estimation will be smaller. Thus finding a lower degree coefficient matrix of Eq. (23) about rotation and observation may be good for the stability of translation estimation.

A. Point-based LiGT

For point correspondences, the relative translation ${}^0 \mathbf{t}_1$ can be given by essential matrix constraints:

$${}^0 \bar{\mathbf{f}}^T \mathbf{E}_{01} {}^1 \bar{\mathbf{f}} = {}^0 \bar{\mathbf{f}}^T [{}^0 \mathbf{t}_1]_{\times} \mathbf{R}_{01} {}^1 \bar{\mathbf{f}} = {}^0 \bar{\mathbf{f}}^T [\mathbf{R}_{01} {}^1 \bar{\mathbf{f}}]_{\times} {}^0 \mathbf{t}_1 = 0, \quad (24)$$

where \mathbf{E}_{01} denotes the essential matrix between frame 0 and frame 1. The $[\mathbf{v}]_{\times}$ denotes the skew-symmetric matrix related to the vector \mathbf{v} . Different from [28], we just consider the essential matrix constraint of relative translation ${}^0 \mathbf{t}_1$, ${}^0 \mathbf{t}_2$, and ${}^1 \mathbf{t}_2$ together and represent these relative translations with global translations, *i.e.* ${}^0 \mathbf{t}_1 = \mathbf{R}_{0G} ({}^G \mathbf{t}_1 - {}^G \mathbf{t}_0)$, ${}^0 \mathbf{t}_2 = \mathbf{R}_{0G} ({}^G \mathbf{t}_2 - {}^G \mathbf{t}_0)$, and ${}^1 \mathbf{t}_2 = \mathbf{R}_{1G} ({}^G \mathbf{t}_2 - {}^G \mathbf{t}_1)$. The coefficient matrices can be obtained by transforming the three essential matrix constraints into the form of LiGT Eq. (23):

$$\begin{aligned} \mathbf{B} &= \begin{bmatrix} -({}^0 \bar{\mathbf{f}}^T [\mathbf{R}_{01} {}^1 \bar{\mathbf{f}}]_{\times} \mathbf{R}_{0G}) \\ -({}^0 \bar{\mathbf{f}}^T [\mathbf{R}_{02} {}^2 \bar{\mathbf{f}}]_{\times} \mathbf{R}_{0G}) \\ \mathbf{0}_{1 \times 3} \end{bmatrix} \\ \mathbf{C} &= \begin{bmatrix} {}^0 \bar{\mathbf{f}}^T [\mathbf{R}_{01} {}^1 \bar{\mathbf{f}}]_{\times} \mathbf{R}_{0G} \\ \mathbf{0}_{1 \times 3} \\ -{}^1 \bar{\mathbf{f}}^T [\mathbf{R}_{12} {}^2 \bar{\mathbf{f}}]_{\times} \mathbf{R}_{1G} \end{bmatrix} \\ \mathbf{D} &= -(\mathbf{B} + \mathbf{C}). \end{aligned} \quad (25)$$

According to Eq. (25), the degree of rotation components and observation components in the coefficient are both equal to 2, which is lower than those in [28] with 3 degrees and 5 degrees, respectively.

B. Line-based LiGT

For lines, according to the trifocal tensor constraints [19],

$$\begin{aligned} \mathbf{0} &= [{}^0 \mathbf{n}]_{\times} [({}^2 \mathbf{t}_0^T {}^2 \mathbf{n}) \mathbf{R}_{01} {}^1 \mathbf{n} - ({}^1 \mathbf{t}_0^T {}^1 \mathbf{n}) \mathbf{R}_{02} {}^2 \mathbf{n}] \\ &= ([{}^0 \mathbf{n}]_{\times} \mathbf{R}_{01} {}^1 \mathbf{n})^2 \mathbf{n}^T {}^2 \mathbf{t}_0 - ([{}^0 \mathbf{n}]_{\times} \mathbf{R}_{02} {}^2 \mathbf{n})^1 \mathbf{n}^T {}^1 \mathbf{t}_0, \end{aligned} \quad (26)$$

we proposed a line-based LiGT. Specifically, we refined the constraints Eq. (26) in two ways. First, we represent the relative translation in the global frame. Second, it is observed that the direction of the vector $([{}^0 \mathbf{n}]_{\times} \mathbf{R}_{01} {}^1 \mathbf{n})$ and the vector $([{}^0 \mathbf{n}]_{\times} \mathbf{R}_{02} {}^2 \mathbf{n})$ are both equal to the line direction represented in the frame 0 (${}^0 \mathbf{r}$) ideally. To mitigate the impact of noise, we retain only the magnitudes of the two vectors and replace their directions with the estimated direction of the line. Thus the coefficient matrices are given below:

$$\begin{aligned} \mathbf{B} &= \text{sgn}({}^0 \mathbf{r}^T [{}^0 \mathbf{n}]_{\times} \mathbf{R}_{01} {}^1 \mathbf{n}) \|[{}^0 \mathbf{n}]_{\times} \mathbf{R}_{01} {}^1 \mathbf{n}\|^2 \mathbf{n}^T \mathbf{R}_{2G} \\ &\quad - \text{sgn}({}^0 \mathbf{r}^T [{}^0 \mathbf{n}]_{\times} \mathbf{R}_{02} {}^2 \mathbf{n}) \|[{}^0 \mathbf{n}]_{\times} \mathbf{R}_{02} {}^2 \mathbf{n}\|^1 \mathbf{n}^T \mathbf{R}_{1G} \\ \mathbf{C} &= \text{sgn}({}^0 \mathbf{r}^T [{}^0 \mathbf{n}]_{\times} \mathbf{R}_{02} {}^2 \mathbf{n}) \|[{}^0 \mathbf{n}]_{\times} \mathbf{R}_{02} {}^2 \mathbf{n}\|^1 \mathbf{n}^T \mathbf{R}_{1G} \\ \mathbf{D} &= -(\mathbf{B} + \mathbf{C}), \end{aligned} \quad (27)$$

where, $\text{sgn}(\cdot)$ is a sign function. When the minimal eigenvalue corresponds to the line direction is large, the line will be removed. Therefore, the value of the sign function in Eq. (27) gets rid of rotation errors and observation noises. The degrees of the rotation and observation components in Eq. (27) are 2 and 3, which are lower than those in the LiGT form proposed by [1], which are 3 and 5, respectively.

C. Translation Part of RT^2PL

For point-line-based LiGT, we use Eq. (25) for point features and Eq. (27) for line features. The Singular Value Decomposition solves the entire linear problem, ensuring speed and independence from the number of features.

IV. EXPERIMENTS

In this section, we first conduct thorough experiments using synthetic data to validate both the fusion strategy and the uncertainty weighting strategy. Simultaneously, the experiments with synthetic data will show the advantages of our method in terms of degeneracy resilience and noise resistance. Then experiments on real-world data will further confirm the accuracy advantages of our method.

A. Experiments in Synthetic Scenes

To evaluate the performance of the proposed methods, we generate synthetic scenes based on the manner in [13]. Three frames are generated, with the first frame fixed. The orientation of the second frame relative to the first is generated using random Euler angles constrained to an absolute value of 0.5 radians. The orientation of the third frame relative to the second one follows the same procedure. The two relative translations between consecutive frames are generated with a uniformly distributed random direction and a maximum magnitude of 2. The 3D point landmarks and the 3D endpoints of the line landmarks are obtained from uniformly distributed random points around the origin of the first frame with a distance between 4 and 8. Simultaneously,

TABLE I
RELATIVE POSE ACCURACY AT DIFFERENT NOISE LEVELS

Cases Noise [pix] Metric [deg]	General case								Planar degeneracy						Pure rotation degeneracy									
	0.5		1.0		1.5		2.0		0.0		0.5		1.0		1.5		0.0		0.5		1.0		1.5	
	e_{rot}	e_t	e_{rot}	e_t	e_{rot}	e_t	e_{rot}	e_t	e_{rot}	e_t	e_{rot}	e_t	e_{rot}	e_t	e_{rot}	e_t	e_{rot}	e_t	e_{rot}	e_t	e_{rot}	e_t	e_{rot}	e_t
7pt [19]/8pt [29] †	0.47	1.10	0.89	2.12	1.36	3.17	1.85	4.37	23.94	110.1	25.43	108.2	25.51	108.0	25.29	110.9	305.8	0.07	0.14	0.22	0.14	0.22	0.46	0.93
5pt-nist [10]	3.32	4.27	3.56	5.87	4.76	6.85	4.86	7.34	6.25	14.52	4.83	12.64	6.00	14.03	5.56	12.89	1.12	0.22	0.46	0.93	1.12	0.22	0.46	0.93
5pt-stew [11]	0.39	0.63	0.68	1.11	1.00	1.61	1.41	2.24	14.12	38.93	4.19	9.55	4.74	10.46	4.60	10.57	73.89	0.19	0.41	0.72	0.19	0.41	0.72	
l-trifocal [19]	2.94	4.26	6.15	8.85	9.10	13.16	12.12	17.70	163.2	115.1	157.0	107.9	155.1	106.7	156.6	108.8	158.4	150.9	151.4	152.2	158.4	150.9	151.4	152.2
p-trifocal [19]	0.37	0.76	0.77	1.59	1.24	2.52	1.57	3.31	24.35	111.4	24.91	108.0	24.83	105.2	24.52	107.4	0.04	0.08	0.14	0.22	0.04	0.08	0.14	0.22
pl-trifocal [19]	0.23	0.45	0.49	0.95	0.72	1.42	0.93	1.88	24.37	111.0	23.20	105.4	23.22	103.1	23.49	106.9	0.07	0.07	0.13	0.21	0.07	0.07	0.13	0.21
NEC [13]	0.20	0.32	0.37	0.61	0.55	0.90	0.71	1.17	0.00	0.00	0.33	0.72	0.57	1.26	0.79	1.71	0.00	0.06	0.13	0.20	0.00	0.06	0.13	0.20
PNEC [14]	0.13	0.22	0.27	0.46	0.40	0.69	0.55	0.97	0.00	0.00	0.22	0.52	0.45	1.06	0.63	1.41	0.00	0.06	0.09	0.15	0.00	0.06	0.09	0.15
NBC (Ours w/o IRLS & Points)	0.28	0.74	0.54	1.58	0.88	2.69	1.19	3.97	0.00	0.00	0.41	1.23	0.86	2.83	1.32	4.79	0.58	0.07	0.13	0.20	0.58	0.07	0.13	0.20
RT ² PL (Ours)	0.07	0.14	0.14	0.27	0.21	0.40	0.29	0.55	0.00	0.00	0.08	0.21	0.16	0.42	0.25	0.64	0.00	0.03	0.05	0.07	0.00	0.03	0.05	0.07

† For fair comparisons, all algorithms conduct their non-minimal version. 7pt falls back to 8pt under this configuration. The experiment at each noise level is repeated 1000 times, and the average values are presented.

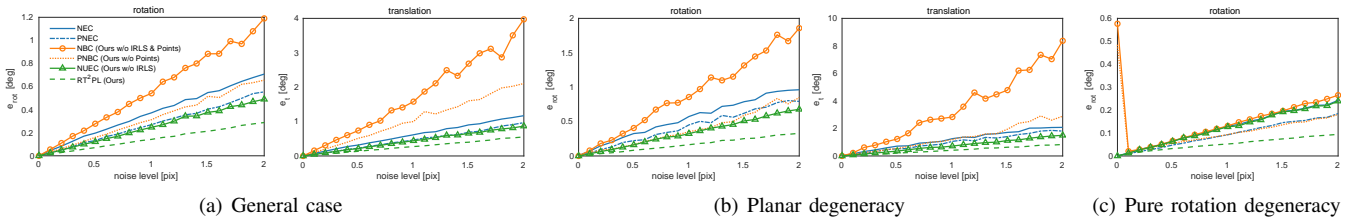


Fig. 2. Ablation experiments. The configuration is set same as Tab I. Each value is averaged over 1000 random experiments.

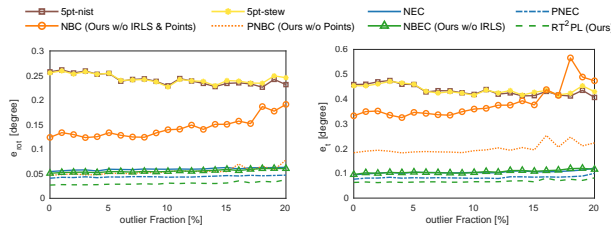


Fig. 3. Convergence and resilience to outliers. 100 random points and 100 random lines are generated for this experiment. All algorithms are embedded into a RANSAC scheme with the same outlier threshold and inlier criteria. Following the manner in [13], the Five features are used as the sample set for 5pt-nist and 5pt-stew. Ten features are used as the sample sets for all non-minimal solvers.

the focal length of the virtual camera is set to 800. Gaussian noise is introduced to perturb each point and each endpoint in images. The standard deviation of Gaussian noise serves as the noise level for both point and line observations. We compare our method on the synthetic scenes to 9 classical or state-of-the-art methods:

- 6 two-view pose estimation methods: namely **5pt-nist** [10], **5pt-stew** [11], **7pt** [19], **8pt** [29], **NEC** [13], and **PNEC** [14].
- 3 three-view pose estimation methods [19]: a line-based trifocal tensor method (**l-trifocal**), a point-based trifocal tensor method (**p-trifocal**), and a point-line-based trifocal tensor method (**pl-trifocal**).

The rotation estimation error metric e_{rot} is defined by the sum of the absolute angle difference of two consecutive relative rotations. The translation estimation error metric e_t is defined by the sum of the absolute angle difference of two consecutive relative translation directions.

Image Noise Resilience and Ablation Test: We generate 15 random points and 15 random lines (for comparing our method to the line-based trifocal tensor method, which needs at least 13 lines, two more lines for trifocal tensor

TABLE II
ESTIMATION TIME WITH 20% OUTLIER FRACTION (MS)

	5pt-stew [11]	NEC [14]	PNEC [14]	NBC (Ours)	PNBC (Ours)	RT ² PL (Ours)
RANSAC*	2.44/38	4.53/63	4.53/63	6.70×2 ¹ /41	6.70×2 ¹ /41	(4.53+6.70)×2 ¹ /63+41
IRLS+Trans. †	-	1.17	1.17	0.46×2 ¹	0.46×2 ¹	1.06×2 ¹
Per relative pose Est.	2.44	4.53	5.70	6.70	7.16	12.29

* Present the time of RANSAC and the number of iterations.

† ×2 means that those methods deal with two relative poses together.

‡ For NEC and NBC, the translation is computed in the RANSAC framework. For PNEC, we need the translation for weighting so that the translation is computed in each loop of IRLS. For lines, we do not need the translation in the loop, therefore, the translation is computed after IRLS.

decomposition) without outliers and add different image noise levels that vary from 0 pixels to 2 pixels. The step size of the noise level is 0.1 pixels. The experiment with an image noise level repeats 1000 times. The optimization in our methods, as well as that in NEC [13] and PNEC [14], are non-convex, making them sensitive to the initial point. We set the starting value for them as a uniform variation around the true rotation as the manner in [13] to ensure that the global minimum is spotted for a proper evaluation of noise resilience. Further discussion about convergence will be shown in the next experiment. To demonstrate the benefits of decoupled estimation, we simulate planar degeneracy cases and pure rotation degeneracy cases by imposing features on a plane and setting translation to zero, respectively.

The results in Tab. I show that the proposed method (RT²PL) outperforms all of the comparative methods. And as the noise level increases, its advantage will be further highlighted. This success is mainly attributed to the incorporation of uncertainty weighting in the cost function and the fusion of points and lines, which can be proven by the results of the ablation experiment shown in Fig 2. Besides, the results demonstrate that methods employing a decoupled estimation scheme (NEC, PNEC, RT²PL) significantly outperform those with mixture parameter problems when degeneracy occurs. It is worth noting that the estimation error with NBC constraints, which also utilizes the decoupled scheme, is not

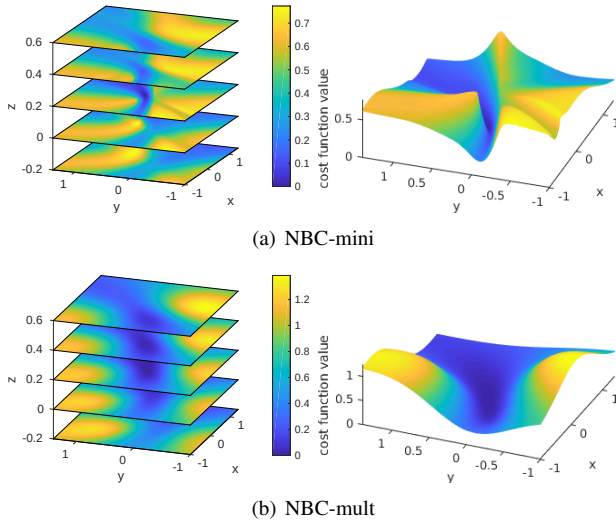


Fig. 4. **Behavior of the NBC cost function.** The testing environment consists of 10 lines and no observation noise is added. Because the cost function involved 6 unknowns, for visualization, we set one relative rotation as the ground truth. We display the values of the cost function as the Cayley parameters of the other rotation change. These parameters take on the ground truth at $[0.2, 0.2, 0.2]$. The right figures display the cost function value changes when $z = 0.2$. The cost function in the multiple form exhibits smoother performance.

zero when the noise level equals zero in pure rotation cases, as shown in the second to last row of Tab. I and Fig. 2(c). It means that NBC cannot handle pure rotation degeneracy cases. It is because when two arbitrary back-projected planes overlap, the position of the third back-projected plane will be unconstrained, i.e. the normals of the back-projected planes of an arbitrary line feature are always coplanar. When the noise level is not zero, the back-projected plane will not strictly overlap which leads to smaller estimation errors. Although NBC is degenerate in pure rotation cases, it can also provide some useful constraints for pose estimation. Thanks to the combination of point and line constraints, the proposed method (RT²PL) gains a significant accuracy improvement compared to PNEC [14] in pure rotation cases.

Convergence and Resilience to Outliers: We employed the RANSAC [30] scheme to enhance the robustness of the proposed algorithms in handling outliers. It is compared with the five-point method [10], [11], NEC [13], and PNEC [14] in a synthetic scene containing 100 points and 100 lines, with up to 20% outliers in each type of measurement. The noise is fixed to 0.5 pixels. For non-convex methods (NEC, PNEC, and all proposed methods), we add random variation in each RANSAC iteration, like that in [13], to try to avoid local minima. The initial value is set to a zero vector. In the case of IRLS-based methods (PNEC, PNBC, RT²PL), the RANSAC scheme is only conducted during the initial loop of IRLS. The results in Fig. 3 show that the random variation scheme is also valid for proposed line-based rotation estimation. Due to the higher sensitivity of line features to noise, as observed in Fig. 2 and Fig. 3, after executing separate RANSAC operations for points and lines for RT²PL, we prefer using the initial estimation generated by point-based RANSAC with random variation when a sufficient number of point

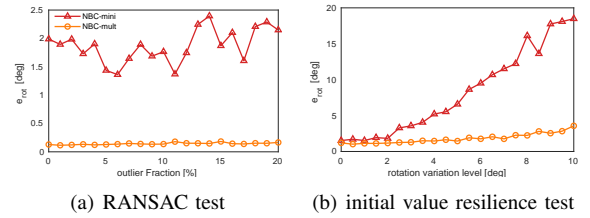


Fig. 5. **Convergence analysis for two NBC forms.** (a) Results of RANSAC with random initialization. The configuration is the same as that for Fig. 3. (b) Initial value resilience test. We set the initial values with deviations ranging from 0° to 10° near the true values to test the algorithm’s convergence without outliers. The noise is fixed to 0.5 pixels.

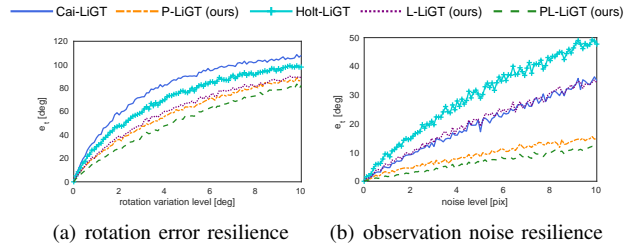


Fig. 6. **Resilience analysis for LiGT.** (a) To assess rotation error resilience, the noise level is set to 0 pixels, and rotation variation ranges from 0° to 10° . (b) To test observation noise resilience, the rotation variation level is fixed as 0° , and the noise level varies from 0 pixels to 10 pixels. Each data point in the plots represents the mean of 1000 trials.

features is available. Then the inliers of points and lines will be used together to produce the initial estimation for the IRLS process.

As mentioned in Sec. II-B, we propose two forms of NBC constraints *i.e.* NBC-mini and NBC-mult. We adopt the NBC-mult as the constraint for the line part in RT²PL. This is because the cost function with NBC-mult constraint has better behavior as outlined in Fig. 4. The results of a further test for convergence of the two forms are shown in Fig. 5. Compared with the NBC-mini form, the NBC-mult form has better resilience to initial value as illustrated in Fig. 5(b). Therefore, as shown in Fig 5(a), NBC-mult will provide more accurate results within the RANSAC framework with the random variation scheme.

Runtime Analysis. To evaluate the running time of the proposed method, we generated a synthetic scene consisting of 100 points and 100 lines, with 20% outliers. The experiments were conducted on an Intel Core i9-13900KS CPU with 32GB of RAM. The results are presented in Table II. While RT²PL takes 12.29 ms for each relative pose estimation, slightly slower than PNEC [14], the optimization process runs in real time and proves to be more efficient than the method proposed in [9], which requires 660 ms for each step of the minimal solver.

Comparison for Translation Estimation: To assess the robustness of the proposed LiGT methods, experiments are conducted in scenes with 10 points and 10 lines. We take the rotation perturbation of ground truth and noisy observation as the input. The results are shown in Fig. 6. The original point-based LiGT [28] and the proposed point-based LiGT are named **Cai-LiGT** and **P-LiGT**, respectively. Line-based LiGT methods corresponding to [1] and Eq. (27) are named **Holt-LiGT** and **L-LiGT**, respectively. The proposed point-

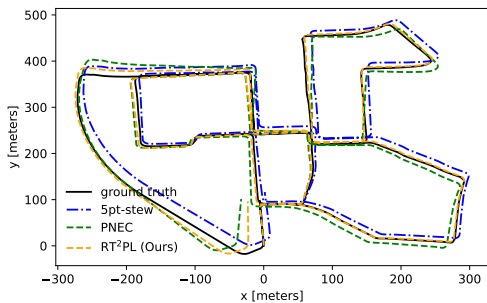


Fig. 7. Trajectory on KITTI Seq. 00

TABLE III

COMPARISON ON KITTI DATASETS

Seq.	5pt-stew [11]		PNEC [14]		RT ² PL (Ours)	
	RRE (°) ↓	RTE (°) ↓	RRE (°) ↓	RTE (°) ↓	RRE (°) ↓	RTE (°) ↓
00	0.136	4.925	0.121	4.561	0.113	3.347
01	1.367	50.605	0.977	45.585	0.505	30.228
02	0.145	2.690	0.106	2.190	0.096	1.998
03	0.086	4.769	0.065	4.952	0.048	1.696
04	0.074	1.131	0.034	0.513	0.036	0.527
05	0.090	9.991	0.062	10.601	0.052	10.407
06	0.082	2.085	0.037	0.836	0.045	1.477
07	0.213	18.660	0.188	18.612	0.154	18.275
08	0.112	8.913	0.062	8.501	0.048	7.965
09	0.086	1.554	0.067	1.643	0.050	1.067
10	0.107	8.582	0.063	5.371	0.060	3.141
Avg.	0.227	10.355	0.162	9.397	0.110	7.284

line-based LiGT is named **PL-LiGT**. As shown in Fig. 6, we can observe that the proposed PL-LiGT exhibits superior performance in both rotation error resilience and observation noise resilience tests. It primarily benefits from the fusion of point and line information and both constraints built by the minimal-degree LiGT. Concurrently, the results reveal that P-LiGT outperforms Cai-LiGT due to the lower degree of rotation and observation. The comparison among line-based LiGT methods yields consistent results. However, the degree metrics become invalid when comparing constraints with different features. For instance, L-LiGT possesses a lower observation components degree than Cai-LiGT, yet both exhibit the equivalent performance in noise resilience. This observation confirms that the line constraints are more sensitive to the observation noise than point constraints.

B. Experiments in Real-world Scenes

In this section, we evaluate the proposed method within a three-frame odometry system on two public datasets, including outdoor datasets (KITTI datasets [31]) and indoor datasets (EuRoC MAV datasets [32]). Before showing the results, we will introduce the implementation details of the odometry system first. We construct a three-frame visual odometry, which means the sliding window size is three, for real-world experiments. For point features, FAST [33] are extracted and tracked by a KLT algorithm [34]. The line features are extracted by the LSD detector [35] and matched by the LBD algorithm [36]. After RANSAC for points and lines, point inliers and line inliers are leveraged together to get the estimation for the first loop of the IRLS solver. The iteration times of IRLS are set to 5. Observation noise for features is set to 1 pixel. We select some algorithms accord-

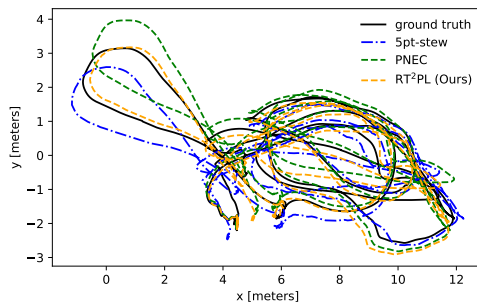


Fig. 8. Trajectory on EuRoC Seq. MH.03

TABLE IV

COMPARISON ON EUROC DATASETS

Seq.	5pt-stew [11]		PNEC [14]		RT ² PL (Ours)	
	RRE (°) ↓	RTE (°) ↓	RRE (°) ↓	RTE (°) ↓	RRE (°) ↓	RTE (°) ↓
MH.01	0.260	11.212	0.163	10.828	0.123	9.992
MH.02	0.301	11.245	0.177	11.242	0.111	9.197
MH.03	0.309	10.772	0.163	7.690	0.115	6.877
MH.04	0.448	12.801	0.261	12.552	0.190	10.806
MH.05	0.418	12.395	0.275	12.099	0.147	10.656
V1.01	0.318	16.940	0.193	16.711	0.208	17.322
V1.02	0.360	15.866	0.240	13.700	0.253	14.371
V1.03	0.567	24.855	0.492	22.404	0.401	21.697
V2.01	0.395	19.181	0.272	17.614	0.303	19.773
V2.02	0.529	23.680	0.402	20.105	0.430	20.810
V2.03	1.758	34.952	1.335	33.268	1.059	34.145
Avg.	0.515	17.627	0.361	16.201	0.304	15.968

ing to their performance on synthetic data for comparison. All these methods are embedded into our odometry system. The estimation methods with non-convex constraints use the same magnitude of variation, set to 0.1 in our system, in each iteration of RANSAC.

Comparison on KITTI Datasets: We use the root mean square errors of relative rotation error and translation direction error to measure the rotation and translation estimation accuracy, respectively. In Tab. III, the middle performance over 5 runs of all approaches is reported. RT²PL outperforms PNEC on 9 out of 11 sequences in rotation and translation accuracy. We attribute this success to the utilization of lines and the proper fusion with points. The clear improvement in Seq.01 underscores this point. Specifically, the presence of similar textures makes numerous incorrect point correspondences. In contrast, the line landmarks on the road and guardrails provide reliable constraints for odometry leading to better performance. Fig. 7 shows trajectories of RT²PL, PNEC [14], and 5pt-stew [11], recovered from the estimated rotation and the estimated translation with true translation scales. The trajectories are aligned with the first pose.

Comparison on EuRoC Datasets: We employ the same metrics to assess the performance of these methods on EuRoC datasets, as shown in Tab. IV for a quantitative comparison. The reconstructed trajectories tested on Seq. MH.03 are depicted in Fig. 8. RT²PL notably enhances estimation accuracy in the sequences of the *MH* series, which contain abundant high-quality lines. However, the incorporation of line features results in a reduction in pose estimation accuracy in the *V* series sequences, primarily due to poor line detection caused by motion blur. Nevertheless, despite this situation, the estimated accuracy has not signifi-

cantly declined, and the overall performance across the entire dataset has improved.

V. CONCLUSION

This paper presents an accurate and real-time algorithm termed RT²PL for three-view pose estimation. Compared to trifocal-tensor-based methods and PNEC, RT²PL improves the accuracy both in general and degenerate cases. This improvement arises from a decoupled pose estimation with a probability-aware point-line-based rotation estimation and an accurate point-line-based linear translation constraint. These results highlight the potential of RT²PL for more accurate initial pose estimation in odometry. Future work will focus on its application in visual-inertial odometry systems.

REFERENCES

- [1] R. J. Holt and A. N. Netravali, "Motion and structure from line correspondences: Some further results," *International Journal of Imaging Systems and Technology*, vol. 5, no. 1, pp. 52–61, 1994.
- [2] R. Gomez-Ojeda, F.-A. Moreno, D. Zuniga-Noël, D. Scaramuzza, and J. Gonzalez-Jimenez, "Pl-slam: A stereo slam system through the combination of points and line segments," *IEEE Transactions on Robotics*, vol. 35, no. 3, pp. 734–746, 2019.
- [3] H. Wei, F. Tang, Z. Xu, and Y. Wu, "Structural regularity aided visual-inertial odometry with novel coordinate alignment and line triangulation," *IEEE Robotics and Automation Letters*, vol. 7, no. 4, pp. 10613–10620, 2022.
- [4] S. Liu, Y. Yu, R. Pautrat, M. Pollefeys, and V. Larsson, "3d line mapping revisited," in *Proceedings of the IEEE/CVF Conference on Computer Vision and Pattern Recognition*, pp. 21445–21455, 2023.
- [5] Y. He, J. Zhao, Y. Guo, W. He, and K. Yuan, "Pl-vio: Tightly-coupled monocular visual-inertial odometry using point and line features," *Sensors*, vol. 18, no. 4, p. 1159, 2018.
- [6] H. Wei, F. Tang, Z. Xu, C. Zhang, and Y. Wu, "A point-line vio system with novel feature hybrids and with novel line predicting-matching," *IEEE Robotics and Automation Letters*, vol. 6, no. 4, pp. 8681–8688, 2021.
- [7] Y. Liu, T. S. Huang, and O. D. Faugeras, "Determination of camera location from 2-d to 3-d line and point correspondences," *IEEE Transactions on pattern analysis and machine intelligence*, vol. 12, no. 1, pp. 28–37, 1990.
- [8] A. Vakhitov, L. Ferraz, A. Agudo, and F. Moreno-Noguer, "Uncertainty-aware camera pose estimation from points and lines," in *Proceedings of the IEEE/CVF Conference on Computer Vision and Pattern Recognition*, pp. 4659–4668, 2021.
- [9] R. Fabbri, T. Duff, H. Fan, M. H. Regan, D. d. C. de Pinho, E. Tsigaridas, C. W. Wampler, J. D. Hauenstein, P. J. Giblin, B. Kimia, et al., "Trplp-trifocal relative pose from lines at points," in *Proceedings of the IEEE/CVF Conference on Computer Vision and Pattern Recognition*, pp. 12073–12083, 2020.
- [10] D. Nistér, "An efficient solution to the five-point relative pose problem," *IEEE transactions on pattern analysis and machine intelligence*, vol. 26, no. 6, pp. 756–770, 2004.
- [11] H. Stewenius, C. Engels, and D. Nistér, "Recent developments on direct relative orientation," *ISPRS Journal of Photogrammetry and Remote Sensing*, vol. 60, no. 4, pp. 284–294, 2006.
- [12] L. Kneip, R. Siegwart, and M. Pollefeys, "Finding the exact rotation between two images independently of the translation," in *Computer Vision—ECCV 2012: 12th European Conference on Computer Vision, Florence, Italy, October 7–13, 2012, Proceedings, Part VI 12*, pp. 696–709, Springer, 2012.
- [13] L. Kneip and S. Lynen, "Direct optimization of frame-to-frame rotation," in *Proceedings of the IEEE International Conference on Computer Vision*, pp. 2352–2359, 2013.
- [14] D. Muhle, L. Koestler, N. Demmel, F. Bernard, and D. Cremers, "The probabilistic normal epipolar constraint for frame-to-frame rotation optimization under uncertain feature positions," in *Proceedings of the IEEE/CVF Conference on Computer Vision and Pattern Recognition*, pp. 1819–1828, 2022.
- [15] C. L. Lawson, "Contribution to the theory of linear least maximum approximation," *Ph. D. dissertation. Univ. Calif.*, 1961.
- [16] C.-K. Chng, A. Parra, T.-J. Chin, and Y. Latif, "Monocular rotational odometry with incremental rotation averaging and loop closure," in *2020 Digital Image Computing: Techniques and Applications (DICTA)*, pp. 1–8, IEEE, 2020.
- [17] A. Concha, M. Burri, J. Briales, C. Forster, and L. Oth, "Instant visual odometry initialization for mobile ar," *IEEE Transactions on Visualization and Computer Graphics*, vol. 27, no. 11, pp. 4226–4235, 2021.
- [18] Y. He, B. Xu, Z. Ouyang, and H. Li, "A rotation-translation-decoupled solution for robust and efficient visual-inertial initialization," in *Proceedings of the IEEE/CVF Conference on Computer Vision and Pattern Recognition*, pp. 739–748, 2023.
- [19] R. Hartley and A. Zisserman, *Multiple view geometry in computer vision*. Cambridge university press, 2003.
- [20] B. Guan, P. Vasseur, and C. Demonceaux, "Trifocal tensor and relative pose estimation from 8 lines and known vertical direction," in *2022 IEEE/RSJ International Conference on Intelligent Robots and Systems (IROS)*, pp. 6001–6008, IEEE, 2022.
- [21] P. Hruby, T. Duff, A. Leykin, and T. Pajdla, "Learning to solve hard minimal problems," in *Proceedings of the IEEE/CVF Conference on Computer Vision and Pattern Recognition*, pp. 5532–5542, 2022.
- [22] Y. Ding, C.-H. Chien, V. Larsson, K. Åström, and B. Kimia, "Minimal solutions to generalized three-view relative pose problem," in *Proceedings of the IEEE/CVF International Conference on Computer Vision*, pp. 8156–8164, 2023.
- [23] A. Morgan, *Solving polynomial systems using continuation for engineering and scientific problems*. SIAM, 2009.
- [24] T. Duff, K. Kohn, A. Leykin, and T. Pajdla, "Plmp-point-line minimal problems in complete multi-view visibility," in *Proceedings of the IEEE/CVF International Conference on Computer Vision*, pp. 1675–1684, 2019.
- [25] R. Fabbri, T. Duff, H. Fan, M. H. Regan, D. d. C. de Pinho, E. Tsigaridas, C. W. Wampler, J. D. Hauenstein, P. J. Giblin, B. Kimia, et al., "Trifocal relative pose from lines at points," *IEEE Transactions on Pattern Analysis and Machine Intelligence*, 2022.
- [26] Z. Xu, H. Wei, F. Tang, Y. Zhang, Y. Wu, G. Ma, S. Wu, and X. Jin, "Plpl-vio: a novel probabilistic line measurement model for point-line-based visual-inertial odometry," in *2023 IEEE/RSJ International Conference on Intelligent Robots and Systems (IROS)*, pp. 5211–5218, IEEE, 2023.
- [27] J. K. Uhlmann, *Dynamic map building and localization: new theoretical foundations*. PhD thesis, University of Oxford, 1995.
- [28] Q. Cai, L. Zhang, Y. Wu, W. Yu, and D. Hu, "A pose-only solution to visual reconstruction and navigation," *IEEE Transactions on Pattern Analysis and Machine Intelligence*, vol. 45, no. 1, pp. 73–86, 2021.
- [29] R. I. Hartley, "In defense of the eight-point algorithm," *IEEE Transactions on pattern analysis and machine intelligence*, vol. 19, no. 6, pp. 580–593, 1997.
- [30] M. A. Fischler and R. C. Bolles, "Random sample consensus: a paradigm for model fitting with applications to image analysis and automated cartography," *Communications of the ACM*, vol. 24, no. 6, pp. 381–395, 1981.
- [31] A. Geiger, P. Lenz, and R. Urtasun, "Are we ready for autonomous driving? the kitti vision benchmark suite," in *2012 IEEE conference on computer vision and pattern recognition*, pp. 3354–3361, IEEE, 2012.
- [32] M. Burri, J. Nikolic, P. Gohl, T. Schneider, J. Rehder, S. Omari, M. W. Achtelik, and R. Siegwart, "The euroc micro aerial vehicle datasets," *The International Journal of Robotics Research*, vol. 35, no. 10, pp. 1157–1163, 2016.
- [33] E. Rosten and T. Drummond, "Machine learning for high-speed corner detection," in *Computer Vision—ECCV 2006: 9th European Conference on Computer Vision, Graz, Austria, May 7–13, 2006. Proceedings, Part I 9*, pp. 430–443, Springer, 2006.
- [34] B. D. Lucas and T. Kanade, "An iterative image registration technique with an application to stereo vision," in *IJCAI'81: 7th international joint conference on Artificial intelligence*, vol. 2, pp. 674–679, 1981.
- [35] R. G. Von Gioi, J. Jakubowicz, J.-M. Morel, and G. Randall, "Lsd: A line segment detector," *Image Processing On Line*, vol. 2, pp. 35–55, 2012.
- [36] L. Zhang and R. Koch, "An efficient and robust line segment matching approach based on lbd descriptor and pairwise geometric consistency," *Journal of visual communication and image representation*, vol. 24, no. 7, pp. 794–805, 2013.